Potassium Ions Promote Electrochemical Nitrogen Reduction on Nano-Au Catalysts Triggered by Bifunctional Boron Supramolecular Assembly

ARTICLE

Potassium Ions Promote Electrochemical Nitrogen Reduction on Nano-Au Catalysts Triggered by Bifunctional Boron Supramolecular Assembly

Xue Zhao,[a] Ziqiong Yang,[a] Artem V. Kuklin,[b,c] Glib V. Baryshnikov,*[b,d] Hans Ågren,[b,e] Wenjing Wang,[f] Xiaohai Zhou*[a,g] and Haibo Zhang*[a,h]

The electrochemical way of reducing nitrogen to ammonia represents green and economic advantages to phrase down irreversible damage caused by the energy-intensive Haber-Bosch process. Here, we introduce an advanced catalyst CB[7]-$K_2[B_{12}H_{12}]$@Au with high dispersed and ultrafine nano-gold. CB[7]-$K_2[B_{12}H_{12}]$@Au electrochemically driven ammonia yield and Faraday efficiency is as high as 41.69 µg h^{-1} $mg_{cat.}^{-1}$ and 29.53% (at -0.4 V *vs* RHE), respectively, reaching US Department of Energy (DOE) utility index of ambient ammonia production along with excellent cycle stability and tolerance that indicates a high potential of industrial practical value. Experimental results and theoretical calculations show that a key to the excellent electrochemical nitrogen reduction performance lies in the smart design of CB[7]-$K_2[B_{12}H_{12}]$@Au catalyst combining the stable substrate anchored Au nanoparticles and K^+ ions that effectively prevent hydrogen evolution reaction and polarizes *N_2 leading to lowering the rate determining stage. This research will promote the further development of electrochemical ammonia with low environmental impact.

Introduction

Ammonia, a chemical that can never be overlooked, covers all aspects of human production and life. The H content in liquid ammonia is as high as 17.6 wt%, and its energy density is close to 13.6 GJ·m^{-3}, making ammonia an emerging green energy carrier.[1-4] Much of the development of modern industry and agriculture is based on the use of ammonia, which is an essential raw material for the manufacture of plastics, fibers, dyes, explosives, resins, pharmaceuticals and artificial fertilizers.[5-8] The Haber-Bosch process using nitrogen and H_2 as raw materials to produce ammonia have established a reliable foundation for mass production of ammonia. The bond energy of the triple bond in N_2 is as high as 940.95 KJ·mol^{-1}, which means that the Haber-Bosch nitrogen fixation process is an energy-intensive process. Therefore, the large-scale production of ammonia is accompanied by a painful price.[9-12] The Haber-Bosch process induced by iron-based catalysis must operate at high temperatures (400-600 °C) and high pressure (150-350 atm.), which accounts for 1 to 2% of the world's annual energy consumption.[13-16] More seriously, the Haber-Bosch process feedstock H_2 is produced by natural gas reformation, which consumes a large amount of fossil fuels and emits a large amount of CO_2 (at least 450 million tons per year), exacerbating greenhouse effects.[13, 16-19] Today, with the rapid development of smart materials and process technology, scientists begin to pay attention to how to convert the N_2 from the atmosphere into ammonia by green and feasible methods under mild conditions to replace the traditional Haber-Bosch process of high energy consumption and environmental cost.

In recent years, the ammonia production process through electrochemical nitrogen reduction reaction (ENRR) has given new hope. The ENRR process can be driven by electricity from solar and wind energy, and the whole process can transform N_2 and H_2O into NH_3 under ambient conditions, enabling distributed sustainable production of ammonia.[20-22] Although ENRR process is considered to be the most promising green ammonia production process, the current research is still at the laboratory exploration stage. Since 2018, researchers have investigated various ENRR catalysts, including single-metal nanomaterials,[2, 15, 23-25] metal oxides,[18, 26-28] metal carbides,[29-32]

[a.] College of Chemistry and Molecular Sciences, Wuhan University, Wuhan 430072, P.R. China
[b.] Division of Theoretical Chemistry and Biology, School of Engineering Sciences in Chemistry, Biotechnology and Health, KTH Royal Institute of Technology, 10691, Stockholm, Sweden
[c.] Department of Science and Innovations, Siberian Federal University, 79 Svobodny av, Krasnoyarsk 660041, Russia
[d.] Department of Chemistry and Nanomaterials Science, Bohdan Khmelnytsky National University, 18031, Cherkasy, Ukraine
[e.] College of Chemistry and Chemical Engineering, Henan University, Kaifeng, Henan 475004, P. R. China
[f.] The State Key Laboratory of Refractories and Metallurgy, School of Chemistry and Chemical Engineering, Wuhan University of Science and Technology, Wuhan 430081, P. R. China
[g.] Engineering Research Center of Organosilicon Compounds & Materials, Ministry of Education, Beijing 100816, P.R. China
[h.] National Demonstration Center for Experimental Chemistry, Wuhan University, Wuhan 430072, P.R. China
* Corresponding author
  Haibo Zhang, E-mail: haibozhang1980@gmail.com
  Xiaohai Zhou, E-mail: zxh7954@whu.edu.cn
  Glib V. Baryshnikov, E mail: glibar@kth.se
†Electronic Supplementary Information (ESI) available: See DOI: 10.1039/x0xx00000x

metal nitrides,[32, 33] metal sulfides,[34-36] and metal-free materials[1, 37-39], and the results of these ENRR catalysts have been greatly inspiring. But researchers have been aware that the ENRR performance of these catalysts is still at the incubation stage of ammonia output and Faraday efficiency (or only one of these two targets can achieve the desired effect), being far from the requirements of industrial production. Single-component ENRR catalysts are often difficult to simultaneously act at every key step of N_2 reduction, while the performance of co-catalysts indicates that the ENRR performance of the target catalyst can be enhanced to some extent.[14, 40] Unfortunately, only limited research has been carried out on ENRR for such regulation engineering. In other words, there is probably still room to further upgrade the performance of existing excellent catalysts and to shorten the exploration period of industrial electrochemical ammonia synthesis under ambient conditions.

In this work, we explore cucurbit[7]uril (CB[7]) and $K_2[B_{12}H_{12}]$ as a stable supramolecular assembly CB[7]-$K_2[B_{12}H_{12}]$ triggered by the "chaotropic effect"[41] as an outside assembly motif, and then harnessing the CB[7]-$K_2[B_{12}H_{12}]$ with bifunctional properties to rapidly obtain a self-supported type of highly dispersed ultrafine nano-gold in situ (CB[7]-$K_2[B_{12}H_{12}]$@Au: as a E-NRR catalyst). The inspiration for this "one stone two birds" strategy comes from: 1) Alkali metal K^+ can change the electronic structure of catalyst surface;[42] 2) Au-based catalyst has an unfilled d orbital that can partially cover the 2p orbital of N, and it is not an effective catalyst for HER reaction; 3) The combination of *closo*-$[B_{12}H_{12}]^{2-}$ and CB[7] driven by chaotropic effect can retain the counter cation (K^+) of *closo*-$[B_{12}H_{12}]^{2-}$; 4) *Closo*-$[B_{12}H_{12}]^{2-}$ has the ability to reduce Au^{3+} to Au^0, after consuming a part of *closo*-$[B_{12}H_{12}]^{2-}$, it can achieve the purpose of in-situ loading of Au on carrier, and the excess part can effectively prevent Au from being oxidized and gathering (or leaching); 5) The binding constant between *closo*-$[B_{12}H_{12}]^{2-}$ and CB[7] is as high as 10^3 M^{-1}, which ensures the stable operation of the catalyst in the electrochemical process. The results of proof-of-concept experiment show that the presence of self-bonding potassium cations greatly enhances the ENRR performance of CB[7]-$K_2[B_{12}H_{12}]$@Au. Compared with most ENRR catalysts (**Figure S1** and **Table S1**), CB[7]-$K_2[B_{12}H_{12}]$@Au simultaneously exhibits high ammonia yield (41.69 μg h^{-1} $mg_{cat.}^{-1}$ or 33.36 μg h^{-1} cm^{-2} at -0.4V *vs* RHE) and Faraday efficiency (29.53%, at -0.4 V *vs* RHE). It is worth noting that the Faraday efficiency of 29.53% reaches the US Department of Energy (DOE) utility index of ambient ammonia production. Stable organic supramolecular assembles not only weaken the HER performance, but also give the excellent stability to nano-Au, which still maintains high catalytic activity after repeated use (8 times) or continuous operation for 20 h. Furthermore, density functional theory (DFT) calculations indicate that the key to superior performance lies in the uniqueness of CB[7]-$K_2[B_{12}H_{12}]$@Au ENRR catalyst design. K^+ effectively prevents H_3O^+ approaching the gold surface due to the repulsion from the positively charged coordination spheres of the K^+ aqua complexes, resulting in a suppression of hydrogen evolution reaction. Simultaneously, the transferred charge enhances the interaction between *N_2 and gold surface that leads to lowering

of the rate-determining state (RDS). Therefore, the marriage of stable substrate-anchored Au nanoparticles with self-bonded K^+ plays a pivotal role in enhancing the competitive reaction selectivity of Au-based catalysts with potential for ENRR, which can promote the further advancement of ambient electrochemical ammonia.

Experimental

Chemicals and materials

Carbon paper (CP) was purchased from Toray Industries, Inc. (Japan) and pre-treated in water/acetone solution with ultrasonic for the ENRR experiments. Nafion-115 proton exchange membranes and Nafion solution (5 wt%) were purchased from DuPont® company (USA). Both high purity Ar and high purity N_2 were purchased from Hubei Harvin (Group) Chemical Co., Ltd., and their purity is above 99.999%. $^{15}N_2$ was purchased from Sigma-Aldrich (purity: 98%; abundance: 98.0%). Ultrapure water (Milli-Q, 18 MΩ cm^{-1}) was used full the entire research process. Other reagents were purchased from Aladdin Chemical Reagent Co., Ltd. (Shanghai, China) and used as received unless otherwise stated.

Materials preparation

Synthesis of CB[7]-$K_2[B_{12}H_{12}]$. First, $[NEt_3H]_2[B_{12}H_{12}]$ was prepared according to the process provided in literature Ref.[43]. Then, potassium-*closo*-dodecaborate ($K_2[B_{12}H_{12}]$) was prepared as follows: 3.4560 g (10 mmol) $[NEt_3H]_2[B_{12}H_{12}]$ was dispersed into 50 mL H_2O, then 0.5610 g (10 mmol) KOH was added (suspension quickly becomes clarified), and the mixed solution was boiled until all H_2O was removed, that is, $K_2[B_{12}H_{12}]$ white solid was obtained. Subsequently, 2.3260 g (2 mmol) of CB[7] and 0.6590 g (3 mmol) of $K_2[B_{12}H_{12}]$ were dissolved in 100 mL H_2O, respectively, and then the two solutions were mixed (with magnetic stirring), and the mixed solution became cloudy immediately. The mixture was stirring continuously for 10 min, and then the precipitate was collected by filtration with ultrapure water washing. The white powder CB[7]-$K_2[B_{12}H_{12}]$ was dried in vacuum at 60 °C for 6 h .

Synthesis of CB[7]-$K_2[B_{12}H_{12}]$@Au. 1.4920 g (1.5 mmol, based on *closo*-$[B_{12}H_{12}]^{2-}$) CB[7]-$K_2[B_{12}H_{12}]$ was re-dispersed in 50 mL H_2O by ultrasound. Then 23.3 mL (24.3 mM) $HAuCl_4$ was added to the suspension (with magnetic stirring), and the suspension changed from bright yellow to purplish red within 1 min. The mixture was stirring continuously for 10 min and stewing the filtrate for 30 min stratification. Then the filtrate was separated and collected by filtration. The pink powder CB[7]-$K_2[B_{12}H_{12}]$@Au was dried in vacuum at 60 °C for 6 h.

Materials characterization

Fourier-transform infrared spectroscopy (FTIR, Thermo iS10, USA) of materials was tested (with potassium bromide as a platform) for qualitative analysis. Powder X-ray diffraction (PXRD, Rigaku Miniflex600, Japan) was used to analysis the

crystal phase composition of materials. Transmission electron microscopy (TEM, HITACHI H-7000FA, Japan) and Field emission scanning electron microscopy (FE-SEM, Zeiss SIGMA, UK) (acceleration voltage: 7.00 kV; signal acquisition mode: In-Lens) were used to inspect the microscopic morphology of materials. X-ray photo-electron spectroscopy (XPS, ESCALAB250Xi, USA) and energy dispersive X-ray spectroscopy based on TEM (TEM-EDAX, JEM-2100F, Japan) were used to qualitatively determine the compositions of the materials. Ultraviolet-visible spectrometry (UV-vis, UV-4802, Unico (Shanghai) Instrument Co., Ltd.) was used to determine content of NH_3 and N_2H_4. Nuclear magnetic resonance spectrometer (Bruker Advance 400 MHz) was used for qualitative detection of $^{15}NH_4$ and Job titration experiments.

Electrochemical measurements

Electrochemical experimental methods refer to our previous work.[44] Typically, the whole ENRR process was performed on an H-type-cell equipped with a three-electrode system (working electrode, reference electrode and counter electrode), the two chambers of H-type cell was separated by a Nafion 115 proton exchange membrane, and cyclic voltammetry data, linear sweep voltammetry data and chronoamperometry data were acquired by an electrochemical workstation (CS 2350, from Wuhan Corrtest Instruments Corp., Ltd., China). More detailed parameters are as follows. Electrolyte: 0.1 M HCl solution; Counter electrode: graphite rod (purity is 99.999 wt%, purchased from Shanghai (China) Jingchong Electronic Technology Development Co. Ltd.); Reference electrode: Ag/AgCl electrode with saturated potassium chloride filling liquid (has been calibrated as 0.197 V by standard hydrogen); Working electrode: CB[7]-$K_2[B_{12}H_{12}]$@Au coated on CP. The working electrode was prepared as follows: 10.0 mg CB[7]-$K_2[B_{12}H_{12}]$@Au was dispersed in "880 μL isopropanol + 120 μL Nafion 5 wt%" mixture solution, then sonicated for 1 h to form a uniform ink. Then 20 μL inks was uniformly coating to the area of 0.5 cm × 0.5 cm on CP and naturally dried. The loading amount of CB[7]-$K_2[B_{12}H_{12}]$@Au on CP is approximately 0.2 mg (or 0.8 mg/cm2). Before each test, the required gas saturated electrolyte was used for 30 min to eliminate other gases in the electrolyte as much as possible. Then 20 times cycles of cyclic voltammetry tests were performed to activate the catalyst (sweep velocity: 100 mV/s), and LSV curves were obtained at a sweep velocity of 5 mV/s. In the ENRR experiment, the electrolyte in the anode cell was saturated with Ar throughout. This work was performed at ambient conditions, and all potentials were recorded by converting the following equation into reversible hydrogen electrode: $E_{RHE} = E_{Ag/AgCl} + 0.059pH + 0.197$. All the polarization data were obtained in conditions of without *iR* correction.

Determination of ammonia

The indophenol blue colorimetric method can be used to accurately detect the ammonia content in an acidic electrolyte.

Specifically, the solution required for colorimetric agent was formulated in the following manner. Solution A: 1 M NaOH solution (containing 5 wt% sodium citrate and 5 wt% salicylic acid); Solution B: 0.05 M NaClO solution (note: NaClO reagent has a great influence on colorimetric experiment, and it must be ensured that the same batch source is used, and that the interval between the first use and the last use is within one month); Solution C: 1 wt% sodium nitroprusside ($CsFeN_6Na_2O·2H_2O$). After the ENRR test was completed, the solution was mixed quickly in the following order: 2 mL electrolyte → 200 μL C solution → 2 mL A solution → 1 mL B solution → stand for 2 h (25 °C). Subsequently, the UV-Vis spectrum (or absorbance at 655 nm) of 550-750 nm was collected. All reported UV-Vis values have been blank corrected, and the colorimetric process and UV-vis spectroscopy tests were repeated three times and the results were given as average values. A series of NH_4Cl standard solutions (0, 0.1, 0.2, 04, 06, 0.8, 1.0, 1.2, 1.4, 1.6 μg mL^{-1}) was prepared with an accurate amount of NH_4Cl, then rapidly mixed in the following order to colorimetric 2 h: 2 mL NH_4Cl standard solution → 200 μL C solution → 2 mL A solution → 1 mL B solution. After the colorimetric completion, the absorbance at 655 nm was detected by UV-Vis, and the relationship between the NH_4Cl standard solution concentration and the absorbance was $y_{(Abs)} = 0.1626x_{([NH_4Cl])} + 0.00001$, which has a good linear relationship ($R^2 = 0.9998$) (**Figure S2**).

Determination of hydrazin

The electrochemical hydrogenation of N_2 may also generate N_2H_4 by-products. Therefore, we used the Watt and Chrisp colorimetric method to determine whether the electrolyte after ENRR contained N_2H_4. Typically, the colorimetric reagent in the Watt and Chrisp colorimetric method is "concentrated hydrochloric acid (30 mL, 12 M) + 300 mL ethanol + 5.9900 g p-(dimethylamino)-benzaldehyde (p-$C_9H_{11}NO$). After the ENRR experiment, 5.0 ml electrolyte and 5.0 ml colorimetric reagent were rapidly mixed and left for 2 h. After the color development was completed, the UV-Vis absorbance was measured at 455 nm, and the N_2H_4 content was obtained by interpolating the UV-Vis standard curve of N_2H_4. A series of concentration gradient standard solutions of N_2H_4 was prepared using an accurate concentration of N_2H_4, and then colorimetrically treated for 2 h according to the above method. The absorbance at 455 nm was obtained by UV-Vis and the relationship between N_2H_4 concentration and absorbance was $y_{(Abs)} = 0.9483x_{([N_2H_4])} + 0.0044$ ($R^2 = 0.9995$), which also had a good linear correlation ($R^2 = 0.9998$) (**Figure S3**).

Ammonia yield and Faraday efficiency calculation details

In ENRR, obtaining a molecule of NH3 requires three electrons, so the Faradaic efficiency can be determined by **Eq.1**. Q_{NH_3} is the amount of charge consumed in NH_3 production, and Q_{total} is the total charge through the electrode. **Eq.2** and **Eq.3** were used to

calculate the rate of NH$_3$ formation, and their units are µg h^{-1} cm^{-2} and µg h^{-1} mg$_{cat.}^{-1}$, respectively.

$$FE(NH_3) = \frac{Q_{NH_3}}{Q_{total}} = \frac{96500 \times 3 \times \frac{[NH_3]}{17} \times V}{1000000 \times \int i\, dt} \quad \text{...} \quad \textbf{Eq.1}$$

$$r(NH_3) = \frac{[NH_3] \times V}{t \times A} \quad \text{...} \quad \textbf{Eq.2}$$

$$r(NH_3) = \frac{[NH_3] \times V}{t \times M_{cat.}} \quad \text{...} \quad \textbf{Eq.3}$$

Here $[NH_3]$ is the mass concentration of NH$_3$ (in µg mL^{-1}), t is the total time (s), V is the volume of electrolyte in cathode chamber (in mL), i is the instantaneous current (in A) of the chronoamperometry test, A is the effective area (in cm^{-2}) of Au/M-BOP coated on CP, and $M_{cat.}$ is the mass of the CB[7]-K$_2$[B$_{12}$H$_{12}$]@Au (in mg).

DFT Calculations

All calculations were carried out within generalized gradient approximation (GGA) of density functional theory (DFT) in the form of Perdew-Burke-Ernzerhof (PBE)[45] exchange-correlation functional as implemented in the VASP code[46, 47]. The D3 method by Grimme[48] was adopted to account for the weak dispersion interactions. A convergence test was performed to determine the optimal plane-wave cutoff energy and the number of Au(111) layers. The cutoff energy of 400 eV and 5 atomic layers of Au (111) 3×3 supercell were so adopted for the NRR simulations. All atoms were relaxed during the simulations. The first Brillouin zone was sampled on a grid of 6×6×1 k-point generated by the Monkhorst-Pack scheme[49]. The periodic images were separated by a vacuum region of at least 16 Å to avoid any interactions between the nearest images along z direction. The convergence criteria of interatomic forces and electronic iterations were set to 10^{-3} eV/Å and 10^{-6} eV, respectively. The effect of unpaired electrons at some steps was treated within spin-polarized calculations.

The Gibbs free energy at each step was calculated at zero potential and pH=0 as $\Delta G = \Delta E + \Delta ZPE - T\Delta S$, where ΔE is the difference in the total energy of product and reagents. ΔZPE and ΔS are the differences in zero-point energy and entropy, respectively, between the adsorbed species and the gas phase molecules. The thermodynamic properties of adsorbed species were calculated using the direct method within the PHONOPY code, while the gas phase values were taken from standard thermochemical tables (at https://janaf.nist.gov/) and Ref.[50]. The half energy of H$_2$ related to (H$^+$ + e) was taken as a reference potential to the standard hydrogen electrode (SHE).

The molecular electrostatic potential for the Au$_{64}$[K(H$_2$O)$_6$]$_4$ model system was calculated by the B3LYP/Lanl2DZ[51-53] method using the Gaussian 16 software [54].

Results and discussion

Closo-[B$_{12}$H$_{12}$]$^{2-}$ is an anion cluster carrying a permanent negative charge of 2e with an icosahedron skeleton by B-B bonds where each B atom is bonded to one H atom. Due to the electron excess, *closo*-[B$_{12}$H$_{12}$]$^{2-}$ exhibits the properties of a reducing agent.[55] *Closo*-[B$_{12}$H$_{12}$]$^{2-}$ can reduce the noble metal ions such as Au^{3+}, Pd^{2+}, Pt^{4+}, Ag$^+$ to the corresponding zero-valent state,[44, 56-58] this process is milder compared to NaBH$_4$. *Closo*-[B$_{12}$H$_{12}$]$^{2-}$ anion cluster possesses a net negative potential on the periphery and can thus interact with the external positive potential of curcubituril[41] or pyridine aromatic[59-61] forming a supramolecular aggregation driven by the "chaotropic effect[62]". As shown in the concept map described in **Figure 1a**, cucurbit[7]uril (CB[7]) and *closo*-[B$_{12}$H$_{12}$]$^{2-}$ quickly combine to form supramolecular aggregates, and then HAuCl$_4$ is introduced to prepare in situ a gold nanocatalyst supported on a specific carrier (CB[7]-K$_2$[B$_{12}$H$_{12}$]@Au). CB[7] and *closo*-[B$_{12}$H$_{12}$]$^{2-}$ have large binding constants, so it is difficult to obtain the crystal structure of CB[7]-K$_2$[B$_{12}$H$_{12}$]. In our previous work, we have found that *closo*-[B$_{12}$H$_{12}$]$^{2-}$ and curcubituril (such as CB[5], CB[6] and CB[8]) can be combined and outsourced through the "chaotropic effect".[41, 57] Based on this, ^{1}H NMR titration
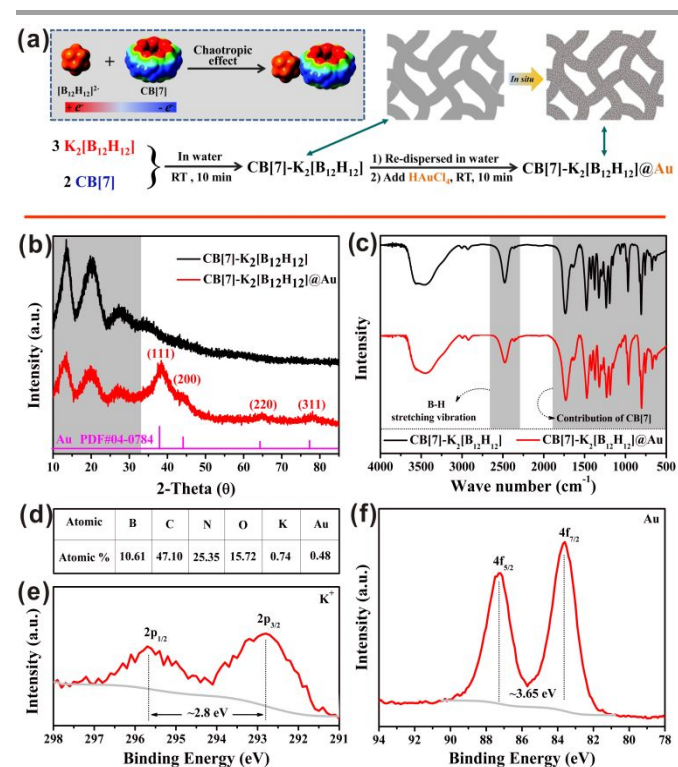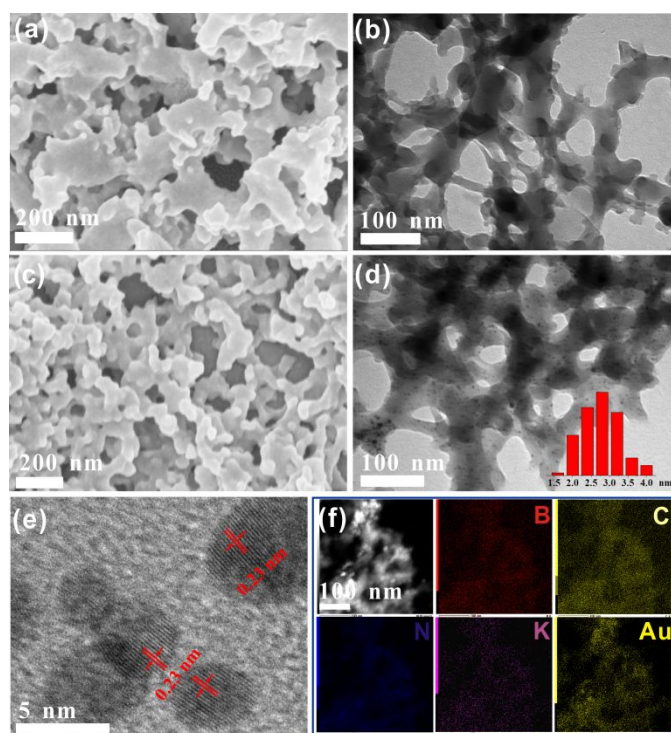

Figure 1. a) Schematic diagram of CB[7]-K$_2$[B$_{12}$H$_{12}$]@Au synthesis; **b)** PXRD results for CB[7]-K$_2$[B$_{12}$H$_{12}$] and CB[7]-K$_2$[B$_{12}$H$_{12}$]@Au; **c)** FT-IR spectrum of CB[7]-K$_2$[B$_{12}$H$_{12}$] and CB[7]-K$_2$[B$_{12}$H$_{12}$]@Au; **d)** XPS semi-quantitative results for each element in CB[7]-K$_2$[B$_{12}$H$_{12}$]@Au; **e)** XPS spectrum of K$^+$ in CB[7]-K$_2$[B$_{12}$H$_{12}$]@Au; and **f)** XPS spectrum of Au in CB[7]-K$_2$[B$_{12}$H$_{12}$]@Au

experiments have determined that the combination ratio of *closo*-[B$_{12}$H$_{12}$]$^{2-}$ and CB[7] is 3:2 (**Figure S4**). In the PXRD spectrum (**Figure 1b**), the peak pattern of the small angle part (10°-30°) in CB[7]-K$_2$[B$_{12}$H$_{12}$]@Au is almost consistent with that of CB[7]-K$_2$[B$_{12}$H$_{12}$], and the new peaks at 38.2°, 44.4°, 64.6° and
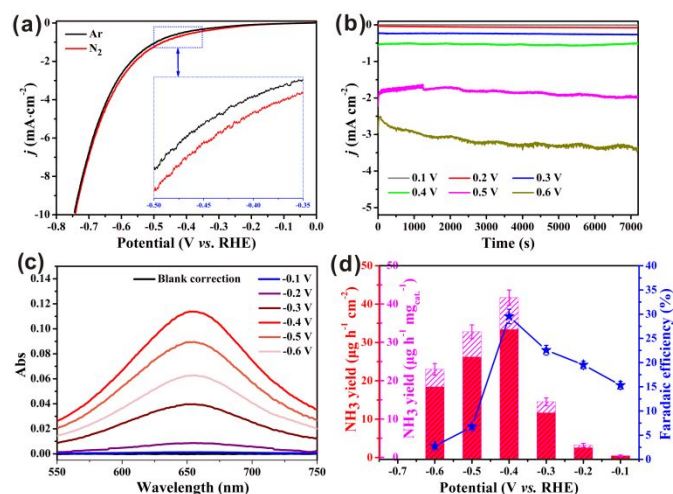
77.5° are consistent with the JPCDS-04-0784 standard card, corresponding to the (111), (200), (220) and (311) crystal plane of Au with face-centered cube structure. This indicates that the structure of carrier CB[7]-K$_2$[B$_{12}$H$_{12}$] can continue to be maintained after that a small dose of *closo*-[B$_{12}$H$_{12}$]$^{2-}$ is consumed in situ, and the stability of this structure origins from the strong binding ability of CB[7] to *closo*-[B$_{12}$H$_{12}$]. FT-IR results (**Figure 1c**) also prove this point, the conversion of CB[7]-K$_2$[B$_{12}$H$_{12}$] to CB[7]-K$_2$[B$_{12}$H$_{12}$]@Au is only manifested in the weakening of the *closo*-[B$_{12}$H$_{12}$]$^{2-}$ characteristic peak (B-H stretching vibration: near 2490 cm^{-1}). In CB[7]-K$_2$[B$_{12}$H$_{12}$]@Au, since CB[7] is electrically neutral, K$^+$ will always adhere to *closo*-[B$_{12}$H$_{12}$]$^{2-}$ as a balanced cation. In XPS, the semi-quantitative results (atomic percentage) of elements B, C, N, O, K and Au were 10.61%, 47.10%, 25.35%, 15.72%, 0.74% and 0.48%, respectively, and the signal peak at 291 eV and 298 eV origines from the contribution of K$^+$2p (**Figure 1d-e**). In addition, the peaks at 83.8 eV and 87.4 eV correspond to 4f$_{7/2}$ and 4f$_{5/2}$ of the zero-valent Au, and the gold elements almost all exist in the form of zero valence in CB[7]-K$_2$[B$_{12}$H$_{12}$]@Au (**Figure 1f**). Electron microscopy can not only present the

Figure 2. **a**) SEM image of CB[7]-K$_2$[B$_{12}$H$_{12}$]; **b**) TEM image of CB[7]-K$_2$[B$_{12}$H$_{12}$]; **c**) SEM image of CB[7]-K$_2$[B$_{12}$H$_{12}$]@Au; **d**) TEM image of CB[7]-K$_2$[B$_{12}$H$_{12}$]@Au; **e**) HRTEM image of CB[7]-K$_2$[B$_{12}$H$_{12}$]@Au; and **f**) Distribution of each element in CB[7]-K$_2$[B$_{12}$H$_{12}$]@Au

transformation of *closo*-[B$_{12}$H$_{12}$]$^{2-}$ to CB[7]-K$_2$[B$_{12}$H$_{12}$]@Au, but also visually present the microscopic morphology of the material. **Figure 2a** and **Figure 2b** are the SEM image and TEM image of CB[7]-K$_2$[B$_{12}$H$_{12}$], respectively, and they both present netlike skeletal structures. As shown in **Figure 2c-d**, the micro-morphology of CB[7]-K$_2$[B$_{12}$H$_{12}$]@Au after HAuCl$_4$ was introduced is almost the same as that of CB[7]-K$_2$[B$_{12}$H$_{12}$], both of which show netlike skeletal structure. The difference is that

in the TEM image of CB[7]-K$_2$[B$_{12}$H$_{12}$]@Au, the netlike skeleton is evenly dispersed with small particles with particle size of about 2.5 nm. The HRTEM image (**Figure 2e**) further identified these dopants with high dispersion and small particle size as Au nanoparticles. In addition, element mapping (**Figure 2f**) also shows that K and Au elements are highly dispersed in CB[7]-K$_2$[B$_{12}$H$_{12}$]@Au. The electron microscope images from CB[7]-K$_2$[B$_{12}$H$_{12}$] to CB[7]-K$_2$[B$_{12}$H$_{12}$]@Au and the high dispersion state of Au in CB[7]-K$_2$[B$_{12}$H$_{12}$]@Au well illustrate the advantages of in-situ preparation of gold nanoparticles using the bifunctional supramolecular aggregates CB[7]-K$_2$[B$_{12}$H$_{12}$] @Au.

The ENRR performance of CB[7]-K$_2$[B$_{12}$H$_{12}$]@Au was evaluated in detail based on the outstanding performance of nano-meter Au catalysts reported in for the electrochemical N$_2$ conversion to ammonia. Electron transfer reactions on the electrode surface often lead to increased current density. Although the flux of N$_2$ electrochemical conversion to ammonia is very small, it can still be used as a preliminary means to evaluate whether a specific catalyst has the potential to promote the ENRR. Under the same conditions, compared with the Ar saturated electrolyte, the LSV curve of the N$_2$ saturated electrolyte shows a higher current density, which indicates that CB[7]-K$_2$[B$_{12}$H$_{12}$]@Au has a certain activation effect on N$_2$ (**Figure 3a**). Based on the LSV curve, the potentiostatic polarization at -0.1 V, -0.2 V, -0.3 V, -0.4 V, -0.5 V, and -0.6 V potentials for 2 h, respectively, their respective curves show a steady trend (**Figure 3b**). The UV-vis spectrum of the electrolyte after indophenol blue colorimetry shows that the absorbance reaches a maximum when the polarization potential was -0.4 V (**Figure 3c**). Based on this result, the ammonia yield of ENRR under the action of CB[7]-K$_2$[B$_{12}$H$_{12}$]@Au reaches 41.69 µg h^{-1} mg$_{cat.}^{-1}$ (or 33.36 µg h^{-1} cm^{-2}) at -0.4 V, which is the optimal result in the applied polarization potential. Combined with the *j*-t curve, the Faraday efficiency under different polarization potential show the characteristics of a "single mountain" type (**Figure 3d**), and the excellent ammonia yield at -0.4 V potential makes the Faraday efficiency as high as 29.53%, which reaches the DOE utility index of ambient ammonia production. When the polarization potential is lower than -0.4 V (in the positive direction), the Faraday efficiency shows a decreasing trend, but the value is still higher than 15%. This is because the HER (competitive reaction) is also weak and the current through the electrode is at a low value, so that the ENRR still accounts for a large proportion. When the polarization potential is

Figure 3. **a**) LSV curves (in the case of Ar and N_2 saturated electrolytes); **b**) j-t curves (chronoamperometry experiment); **c**) UV-vis spectrum of electrolyte after colorimetric for 2 h; **d**) Ammonia yield and Faraday efficiency at different potentials

higher than -0.4 V (negative direction), the Faraday efficiency shows a "cliff-like" drop. This is due to the sensitivity of the HER to the polarization potential, which makes it an absolute advantage at high overpotentials. Even though the ammonia yield here only decreases slightly compared to -0.4 V, the proportion of ENRR has been greatly reduced in a competitive environment. In addition, the presence of N_2H_4 is almost undetectable in the electrolyte (no response from UV-vis), so the electrochemical reduction path of N_2 on CB[7]-K_2[$B_{12}H_{12}$]@Au is considered to be specific. To further locate the active center of ENRR, the ENRR performance were tested, respectively, with "carbon paper (CP)", "CB[7]-K_2[$B_{12}H_{12}$] on CP", "CB[7]-Na_2[$B_{12}H_{12}$]@Au on CP", and "CB[7]-K_2[$B_{12}H_{12}$] @Au on CP" as a working electrode. As shown in **Figure 4a**, when CP was used as the working electrode, the ammonia yield was extremely low, only 1.71 µg h^{-1} mg$_{cat.}$$^{-1}$, while "CB[7]-$K_2$[$B_{12}H_{12}$] on CP" had almost no gain relative to CP. We noticed that "CB[7]-Na_2[$B_{12}H_{12}$]@Au on CP" or "CB[7]-K_2[$B_{12}H_{12}$]@Au on CP" as the working electrode both showed significant ENRR performance; and compared with "CB[7]-Na_2[$B_{12}H_{12}$]@Au on CP", the ENRR performance of "CB[7]-K_2[$B_{12}H_{12}$]@Au on CP" is more significant. Based on this, we can say that the synergistic effect of nano-Au and alkali metal ions in the ENRR process promotes the conversion of N_2 to ammonia, and the promotion effect of K^+ is more obvious than that of Na^+. At present, the production of N_2 into ammonia by electrochemical methods is still at the microgram level. Therefore, in addition to the strict environmental pollution pretreatment (including atmospheric environment, experimental equipment and chemical reagent), a $^{15}N_2$ isotope labeling experiment is necessary.[63] With $^{15}N_2$ as the electrolyte filling gas, the electrolyte after the potentiostatic polarization (after concentration) shows two peaks of equal intensity (J = 73 Hz) in ^{1}HNMR (δ6.9-δ7.25) (**Figure 4b**), corresponding to the characteristics peak type of $^{15}NH_4^+$, while $^{14}NH_4^+$ in this range will appear as three peaks of equal intensity

(J = 52 Hz). Therefore, almost all of the ammonia comes from the conversion of N_2 on the CB[7]-K_2[$B_{12}H_{12}$]@Au electrocatalyst.

Stability is a crucial criterion in evaluating the comprehensive performance of a catalyst. At the optimum potential (-0.4 V), after CB[7]-K_2[$B_{12}H_{12}$]@Au was reused 10 times, its performance was still at a high level, and the ammonia yield and Faraday efficiency fluctuated only slightly near the initial values (**Figure 4c**). In addition, the electrode equipped with CB[7]-K_2[$B_{12}H_{12}$]@Au operates for a long time of 20 h, and the current density (j) hardly fluctuates with time (t), indicating that CB[7]-K_2[$B_{12}H_{12}$]@Au has excellent electrochemical durability (**Figure 4d**). In addition, the changes of physical and chemical properties of CB[7]-K_2[$B_{12}H_{12}$]@Au after use can be almost ignored, which was shown in the FT-IR, XRD, SEM images and in the TEM image (**Figure S5-S8**). The excellent chemical stability of CB[7]-K_2[$B_{12}H_{12}$]@Au is closely related to its own properties: 1) The strong supramolecular interaction (chaotropic effect) between CB[7] and *closo*-[$B_{12}H_{12}$]$^{2-}$ determines that the carrier in CB[7]-K_2[$B_{12}H_{12}$]@Au has good stability; 2) Utilizing the weak reducing property of *closo*-[$B_{12}H_{12}$]$^{2-}$, the in-situ prepared nano-Au is tightly confined within the framework, avoiding the aggregation and leaching of nano-Au during the catalysis process; 3) Zero-valent nano Au has a tendency to accept electrons. Under the permanent negative charge atmosphere carried by *closo*-[$B_{12}H_{12}$]$^{2-}$ itself, nano Au cannot easily escape from the carrier. All in all, the excellent electrochemical nitrogen fixation performance and long-term stability have given CB[7]-K_2[$B_{12}H_{12}$]@Au high-efficiency and economic characteristics, so it is expected the possibility going from laboratory to actual production can be realized.

The density functional theory calculations were carried out to reveal how the presence of potassium can affect the NRR process. Previously it has been demonstrated that NRR on
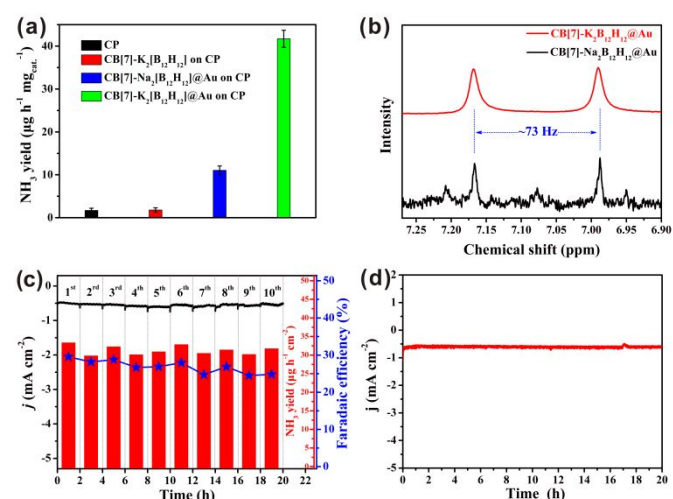
Figure 4. **a**) ENRR active site confirmation test in CB[7]-K_2[$B_{12}H_{12}$]@Au; **b**) ^{1}H NMR results of isotope labeling experiments; **c**) Ammonia production and Faraday efficiency at each recycle; **d**) j-t curve of CB[7]-K_2[$B_{12}H_{12}$]@Au working continuously for 20 h
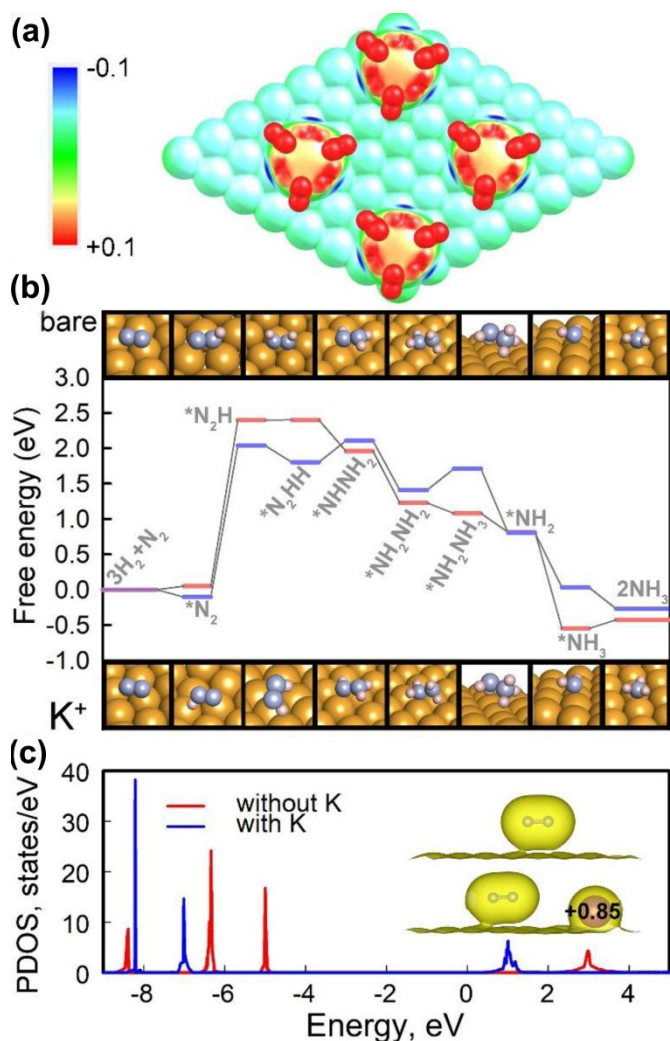
Figure 5. **a**) Molecular electrostatic potential map of four $[K(H_2O)_6]$ on Au(111) surface generated with B3LYP/Lanl2DZ level. The red surface corresponds to a positively charged region of electrostatic potential (+0.1 a.u.), whereas the blue one represents the region with negative potential (-0.1 a.u.). (**b**) Comparative Gibbs free energy diagram of the electrochemical reduction of N_2 to NH_3 on the bare (red) and K-doped (blue) Au(111) surface at 300 K. (pH 0 and U = 0 V versus SHE). Corresponding optimized structures are shown in the insets. (**c**) Projected density of states (PDOS) on nitrogen orbitals without (red) and with (blue) K atom. The inset shows spatial distribution electron density in the interface area of potassium-free (top) and potassium-doped gold (111) surface.

Au(111) would follow the associative mechanism where the first protonation of N_2 to *NNH is a rate-determining step (RDS)[13, 15, 64, 65]. In general, the ENRR is always accompanied by a hydrogen evolution reaction (HER), which is a competing reaction that affects the efficiency of the whole NRR process. Though gold is considered as HER active, its activity with respect to hydrogen evolution can be greatly reduced by adding K ions[40, 66, 67].

It was previously established[40, 66, 67] that the adsorption of K^+ ions on the Au surface creates a kinetic barrier for the diffusion of H_3O^+ ions to the Au substrate. In order to prove this idea, we have performed simulations of the molecular electrostatic potential for a fragment of Au(111) surface covered by four $[K(H_2O)_6]$ complexes (**Figure 5a**). The whole system was considered electroneutral but strongly polarized. We assume that the CB[7]-$K_2[B_{12}H_{12}]$@Au composite may dissociate like a

slat at the interface with water and that the resulting K^+ ions immediately are hydrated by six water molecules, that have previously been shown in numerous theoretical and experimental studies[68-71]. It is found that in our model each $[K(H_2O)_6]$ complex donates one electron to the gold surface that corresponds to the real conditions of NRR (i.e. in real NRR cell the Au(111) surface gains negative charge by the applied bias, while the $[K(H_2O)_6]^+$ exists in the solution[40, 41, 43, 44]). One can see from **Figure 5a**, that the $[K(H_2O)_6]^+$ complexes provide an efficient covering of the gold surface by creating a wide area of a positive electrostatic potential (PEP) over the surface. The PEP is mainly localized on the three outer water molecules of the second hydration shell of the K atom. These three molecules are not directly coupled to the K atom, but are strongly bound and polarized through the H-bond network between them and by the other three water molecules in the first coordination shell of the K atom. Taking into account the effective vdW radius of H atoms and the circle-shaped structure of $[K(H_2O)_6]$ we have estimated that four $[K(H_2O)_6]$ complexes cover 50% of the designed surface fragment containing 64 Au atoms. Since the $[K(H_2O)_6]$ complexes partially cover some Au atoms, the number of uncovered Au active sites able to adsorb H_3O^+ ions responsible for hydrogen evolution is even smaller (about 16 atoms or 25%). At the same time, adsorption of neutral N_2 molecules is indifferent to the PEP over the surface, i.e. the adsorbed $[K(H_2O)_6]$ species selectively prevent the approach of the positively-charged ions to the active surface, but do not prevent penetration of neutral N_2 species. Thus, the adsorbed K^+ ion can indeed kinetically suppress the HER process that makes it possible to observe NRR at higher applied potentials, therefore, improving the ammonia yield.

Besides the kinetic factor, the calculated Gibbs free energy diagram (**Figure 5b**) shows that the adsorbed K atoms lower the energy of N_2 reduction to NH_3. In particular, the adsorption of the N_2 molecule on the K-doped Au(111) surface becomes stronger compared to bare gold due to enhanced surface electron density caused by charge transfer from K to the top layer of Au(111). This results in a more effective overlap between surface d-orbitals and adsorbed N_2 p-orbitals (**Figure 5c**, inset) lowering the free energy from +0.05 eV to -0.10. The N_2 projected density of states (**Figure 5c**) clearly show a shift of nitrogen orbitals to lower energies caused by accepted charge transfer from K atoms to the gold surface and then to the nitrogen, therefore suggesting a stronger acceptor character of N_2 in the presence of potassium cations. The excess surface charge effectively polarizes nitrogen resulting in lowering the energy of the next step. The adsorbed K atom stabilizes the RDS intermediate (*N_2H) by 0.29 eV (at 0 V vs SHE, pH 0), which is similar to the recent results found in Ref.[40] (0.22 eV). After that, *NHNH intermediate is formed with energy decrease by 0.24 eV relatively to the the previous step (**Figure 5b**). While some of the next stages lift the energy up a bit, the energy of the whole reaction falls down and a desorption of NH_3 species occurs without any energy barrier.

ARTICLE

To highlight, potassium cations effectively prevent H_3O^+ approaching the gold surface due to the repulsion from the positively charged coordination sphere of the K^+ aqua complexes resulting in a suppression of the hydrogen evolution reaction. Simultaneously, the transferred charge enhances the interaction between $*N_2$ and the gold surface that leads to lower RDS. Generally, such a dual effect of K^+ ions can be utilized for any HER-active metal surfaces able to trap K^+ ions upon ENRR conditions.

Conclusions

An advanced ENRR catalyst with in-situ loaded high-dispersion ultra-fine nano-gold supported by the dual-functional carrier $CB[7]$-$K_2[B_{12}H_{12}]$ was constructed and analyzed in this work. $CB[7]$-$K_2[B_{12}H_{12}]@Au$ achieves an effective electrochemical reduction of nitrogen to ammonia under ambient conditions, with an ammonia yield and Faraday efficiency as high as 41.69 $\mu g\ h^{-1}\ mg_{cat.}^{-1}$ and 29.53% (at -0.4 V vs RHE), respectively. The chaotropic effect drives $CB[7]$ and $K_2[B_{12}H_{12}]$ to form stable functional carriers $CB[7]$-$K_2[B_{12}H_{12}]$ with Au nanoparticles anchored in situ, so guaranteeing an excellent cyclic stability and tolerance of $CB[7]$-$K_2[B_{12}H_{12}]$. Experimental results and theoretical calculations clarify that the key to the excellent ENRR performance lies in the design of the $CB[7]$-$K_2[B_{12}H_{12}]@Au$ catalyst, and in the combination of stable substrate anchored Au nanoparticles and self-bonding K^+ ions. This finding highlights the potential of the Au-based catalysts with prospects for ENRR, and which, we believe, constitutes a significant step in the development of environmentally friendly and effective electrochemical ammonia.

Conflicts of interest

There are no conflicts to declare.

Acknowledgements

Notes and references

1. W. Qiu, X.-Y. Xie, J. Qiu, W.-H. Fang, R. Liang, X. Ren, X. Ji, G. Cui, A. M. Asiri, G. Cui, B. Tang and X. Sun, *Nat. Commun.,* 2018, **9**, 3485.

2. J. Zheng, Y. Lyu, M. Qiao, J. P. Veder, R. D. Marco, J. Bradley, R. Wang, Y. Li, A. Huang, S. P. Jiang and S. Wang, *Angew. Chem., Int. Ed.*, 2019, **58**, 18604-18609.

3. L. Li, C. Tang, B. Xia, H. Jin, Y. Zheng and S.-Z. Qiao, *ACS Catal.*, 2019, **9**, 2902-2908.

4. J. Zheng, Y. Lyu, M. Qiao, R. Wang, Y. Zhou, H. Li, C. Chen, Y. Li, H. Zhou, S. P. Jiang and S. Wang, *Chem*, 2019, **5**, 617-633.

5. P. Chen, N. Zhang, S. Wang, T. Zhou, Y. Tong, C. Ao, W. Yan, L. Zhang, W. Chu, C. Wu and Y. Xie, *Proc. Natl. Acad. Sci.*, 2019, **116**, 6635.

6. R. Schlögl, *Angew. Chem., Int. Ed.,* 2003, **42**, 2004-2008.

7. V. Rosca, M. Duca, M. T. de Groot and M. T. M. Koper, *Chem. Rev.*, 2009, **109**, 2209-2244.

8. X. Zhang, T. Wu, H. Wang, R. Zhao, H. Chen, T. Wang, P. Wei, Y. Luo, Y. Zhang and X. Sun, *ACS Catal.*, 2019, **9**, 4609-4615.

9. Z. Geng, Y. Liu, X. Kong, P. Li, K. Li, Z. Liu, J. Du, M. Shu, R. Si and J. Zeng, *Adv. Mater.*, 2018, **30**, 1803498.

10. S. Wang, X. Hai, X. Ding, K. Chang, Y. Xiang, X. Meng, Z. Yang, H. Chen and J. Ye, *Adv. Mater.*, 2017, **29**, 1701774.

11. X. Chen, N. Li, Z. Kong, W.-J. Ong and X. Zhao, *Mater. Horiz.*, 2018, **5**, 9-27.

12. C. J. M. van der Ham, M. T. M. Koper and D. G. H. Hetterscheid, *Chem. Soc. Rev.*, 2014, **43**, 5183-5191.

13. D. Bao, Q. Zhang, F.-L. Meng, H.-X. Zhong, M.-M. Shi, Y. Zhang, J.-M. Yan, Q. Jiang and X.-B. Zhang, *Adv. Mater.*, 2017, **29**, 1604799.

14. G.-F. Chen, X. Cao, S. Wu, X. Zeng, L.-X. Ding, M. Zhu and H. Wang, *J. Am. Chem. Soc.*, 2017, **139**, 9771-9774.

15. J. Wang, L. Yu, L. Hu, G. Chen, H. Xin and X. Feng, *Nat. Commun.*, 2018, **9**, 1795.

16. X. Yu, P. Han, Z. Wei, L. Huang, Z. Gu, S. Peng, J. Ma and G. Zheng, *Joule*, 2018, **2**, 1610-1622.

17. M.-M. Shi, D. Bao, B.-R. Wulan, Y.-H. Li, Y.-F. Zhang, J.-M. Yan and Q. Jiang, *Adv. Mater.*, 2017, **29**, 1606550.

18. M. Nazemi, S. R. Panikkanvalappil and M. A. El-Sayed, *Nano Energy*, 2018, **49**, 316-323.

19. J. Han, Z. Liu, Y. Ma, G. Cui, F. Xie, F. Wang, Y. Wu, S. Gao, Y. Xu and X. Sun, *Nano Energy*, 2018, **52**, 264-270.

20. C. Lv, Y. Qian, C. Yan, Y. Ding, Y. Liu, G. Chen and G. Yu, *Angew. Chem., Int. Ed.*, 2018, **57**, 10246-10250.

21. X. Yang, J. Nash, J. Anibal, M. Dunwell, S. Kattel, E. Stavitski, K. Attenkofer, J. G. Chen, Y. Yan and B. Xu, *J. Am. Chem. Soc.*, 2018, **140**, 13387-13391.

22. C. Tang and S.-Z. Qiao, *Chem. Soc. Rev.*, 2019, **48**, 3166-3180.

23. Y.-X. Lin, S.-N. Zhang, Z.-H. Xue, J.-J. Zhang, H. Su, T.-J. Zhao, G.-Y. Zhai, X.-H. Li, M. Antonietti and J.-S. Chen, *Nat. Commun.*, 2019, **10**, 4380.

24. Y. Yao, H. Wang, X.-z. Yuan, H. Li and M. Shao, *ACS Energy Lett.*, 2019, **4**, 1336-1341.

25. D. Yang, T. Chen and Z. Wang, *J. Mater. Chem. A*, 2017, **5**, 18967-18971.

26. C. Lv, C. Yan, G. Chen, Y. Ding, J. Sun, Y. Zhou and G. Yu, *Angew. Chem., Int. Ed.*, 2018, **57**, 6073-6076.

27. W. Kong, F. Gong, Q. Zhou, G. Yu, L. Ji, X. Sun, A. M. Asiri, T. Wang, Y. Luo and Y. Xu, *J. Mater. Chem. A*, 2019, **7**, 18823-18827.

28. H. Du, X. Guo, R.-M. Kong and F. Qu, *Chem. Commun.,* 2018, **54**, 12848-12851.

29. G. Yu, H. Guo, S. Liu, L. Chen, A. A. Alshehri, K. A. Alzahrani, F. Hao and T. Li, *ACS Appl. Mater. Interfaces*, 2019, **11**, 35764-35769.

30. G. Yu, H. Guo, W. Kong, T. Wang, Y. Luo, X. Shi, Abdullah M. Asiri, T. Li and X. Sun, *J. Mater. Chem. A*, 2019, **7**, 19657-19661.

31. H. Cheng, L.-X. Ding, G.-F. Chen, L. Zhang, J. Xue and H. Wang, *Adv. Mater.*, 2018, **30**, 1803694.

32. Y. Wang, X. Cui, J. Zhao, G. Jia, L. Gu, Q. Zhang, L. Meng, Z. Shi, L. Zheng, C. Wang, Z. Zhang and W. Zheng, *ACS Catal.*, 2019, **9**, 336-344.

33. H. Jin, L. Li, X. Liu, C. Tang, W. Xu, S. Chen, L. Song, Y. Zheng and S.-Z. Qiao, *Adv. Mater.*, 2019, **31**, 1902709.

34. L. Zeng, S. Chen, J. van der Zalm, X. Li and A. Chen, *Chem. Commun.*, 2019, **55**, 7386-7389.

35. L. Zhang, X. Ji, X. Ren, Y. Ma, X. Shi, Z. Tian, A. M. Asiri, L. Chen, B. Tang and X. Sun, *Adv. Mater.*, 2018, **30**, 1800191.

36. P. Li, W. Fu, P. Zhuang, Y. Cao, C. Tang, A. B. Watson, P. Dong, J. Shen and M. Ye, *Small*, 2019, **15**, 1902535.

37. X. Zhu, T. Wu, L. Ji, C. Li, T. Wang, S. Wen, S. Gao, X. Shi, Y. Luo, Q. Peng and X. Sun, *J. Mater. Chem. A*, 2019, **7**, 16117-16121.

38. L. Zhang, L.-X. Ding, G.-F. Chen, X. Yang and H. Wang, *Angew. Chem., Int. Ed.*, 2019, **58**, 2612-2616.

39. C. Chen, D. Yan, Y. Wang, Y. Zhou, Y. Zou, Y. Li and S. Wang, *Small*, 2019, **15**, 1805029.

40. Y.-C. Hao, Y. Guo, L.-W. Chen, M. Shu, X.-Y. Wang, T.-A. Bu, W.-Y. Gao, N. Zhang, X. Su, X. Feng, J.-W. Zhou, B. Wang, C.-W. Hu, A.-X. Yin, R. Si, Y.-W. Zhang and C.-H. Yan, *Nat. Catal.*, 2019, **2**, 448-456.

41. W. Wang, X. Wang, J. Cao, J. Liu, B. Qi, X. Zhou, S. Zhang, D. Gabel, W. M. Nau, K. I. Assaf and H. Zhang, *Chem. Commun.*, 2018, **54**, 2098-2101.

42. G. Ertl, D. Prigge, R. Schloegl and M. Weiss, *J. Catal.*, 1983, **79**, 359-377.

43. A. I. Wixtrom, Y. Shao, D. Jung, C. W. Machan, S. N. Kevork, E. A. Qian, J. C. Axtell, S. I. Khan, C. P. Kubiak and A. M. Spokoyny, *Inorg. Chem. Front.*, 2016, **3**, 711-717.

44. X. Zhao, C. Yao, H. Chen, Y. Fu, C. Xiang, S. He, X. Zhou and H. Zhang, *J. Mater. Chem. A*, 2019, **7**, 20945-20951.

45. J. P. Perdew, K. Burke and M. Ernzerhof, *Phys. Rev. Lett.*, 1996, **77**, 3865-3868.

46. G. Kresse and J. Furthm Uller, *Phys. Rev. B*, 1996, **54**, 11169-11186.

47. G. Kresse and J. Hafner, *Phys. Rev. B*, 1993, **47**, 558-561.

48. S. Grimme, *J. Comput. Chem.*, 2006, **27**, 1787-1799.

49. H. J. Monkhorst and J. D. Pack, *Phys. Rev. B*, 1976, **13**, 5188-5192.

50. K. K. Irikura, *J. Phys. Chem. Ref. Data*, 2009, **38**, 749-749.

51. A. D. Becke, *J. Chem. Phys.*, 1993, **98**, 5648-5652.

52. P. J. Hay and W. R. Wadt, *J. Chem. Phys.*, 1985, **82**, 270-283.

53. C. Lee, W. Yang and R. G. Parr, *Phys. Rev. B*, 1988, **37**, 785-789.

54. M. J. Frisch, G. W. Trucks, H. B. Schlegel, G. E. Scuseria, M. A. Robb, J. R. Cheeseman, G. Scalmani, V. Barone, G. A. Petersson and Nakatsuji.

55. N. Jiao, Y. Zhang, L. Liu, J. n. M. Shreeve and S. Zhang, *J. Mater. Chem. A*, 2017, **5**, 13341-13346.

56. X. Zhao, Y. Fu, C. Yao, S. Xu, Y. Shen, Q. Ding, W. Liu, H. Zhang and X. Zhou, *ChemCatChem*, 2019, **11**, 2362-2369.

57. B. Qi, X. Li, L. Sun, B. Chen, H. Chen, C. Wu, H. Zhang and X. Zhou, *Nanoscale*, 2018, **10**, 19846-19853.

58. X. Zhao, Z. Yang, W. Wang, Y. Li, X. Zhou and H. Zhang, *J. Mater. Chem. A*, 2020.

59. X. Zhao, D. Wang, C. Xiang, F. Zhang, L. Liu, X. Zhou and H. Zhang, *ACS Sustainable Chem. Eng.*, 2018, **6**, 16777-16787.

60. X. Zhao, C. Xiang, F. Zhang, F. Yao, R. Sheng, Q. Ding, W. Liu, H. Zhang and X. Zhou, *ACS Appl. Mater. Interfaces*, 2019, **11**, 43214-43222.

61. X. Zhao, F. Zhang, H. Chen, R. Sheng, G. V. Baryshnikov, H. Ågren, X. Zhou and H. Zhang, *Chem. Eng. J.*, 2020, **385**, 123827.

62. K. I. Assaf and W. M. Nau, *Angew. Chem., Int. Ed.*, 2018, **57**, 13968-13981.

63. B. H. R. Suryanto, H.-L. Du, D. Wang, J. Chen, A. N. Simonov and D. R. MacFarlane, *Nat. Catal.*, 2019, **2**, 290-296.

64. J. H. Montoya, C. Tsai, A. Vojvodic and J. K. Nørskov, *ChemSusChem*, 2015, **8**, 2180-2186.

65. Z.-H. Xue, S.-N. Zhang, Y.-X. Lin, H. Su, G.-Y. Zhai, J.-T. Han, Q.-Y. Yu, X.-H. Li, M. Antonietti and J.-S. Chen, *J. Am. Chem. Soc.*, 2019, **141**, 14976-14980.

66. Q. Zhang, B. Liu, L. Yu, Y. Bei and B. Tang, *ChemCatChem*, 2020, **12**, 334-341.

67. T.-A. Bu, Y.-C. Hao, W.-Y. Gao, X. Su, L.-W. Chen, N. Zhang and A.-X. Yin, *Nanoscale*, 2019, **11**, 10072-10079.

68. J. Mähler and I. Persson, *Inorg. Chem.*, 2012, **51**, 425-438.

69. E. D. Glendening and D. Feller, *J. Phys. Chem.*, 1995, **99**, 3060-3067.

70. H. M. Lee, J. Kim, S. Lee, B. J. Mhin and K. S. Kim, *J. Phys. Chem.*, 1999, **111**, 3995-4004.

71. J. S. Rao, T. C. Dinadayalane, J. Leszczynski and G. N. Sastry, *J. Phys. Chem. A*, 2008, **112**, 12944-12953.

Table of Content: The development of sustainable ambient electrochemical nitrogen reduction to produce ammonia instead of the harsh H-B process has become the goal pursued by human beings, where the alkali metal potassium ion can

effectively improve the E-NRR activity of Au anchored on the functional carrier.